Ocean Sci. Discuss., 9, 63–103, 2012
www.ocean-sci-discuss.net/9/63/2012/
doi:10.5194/osd-9-63-2012

Ocean Science Discussions

The analysis of large-scale turbulence characteristics in the Indonesian seas derived from a regional model based on the Princeton Ocean Model

K. O'Driscoll[1] **and V. Kamenkovich**[2]

[1]Institute of Oceanography, Centre for Marine and Atmospheric Sciences, University of Hamburg, Bundesstrasse 53, 20146 Hamburg, Germany
[2]Department of Marine Science, The University of Southern Mississippi, Stennis Space Center, MS 39529, USA

Received: 6 December 2011 – Accepted: 20 December 2011 – Published: 16 January 2012

Correspondence to: K. O'Driscoll (kieran.odriscoll@zmaw.de)

Published by Copernicus Publications on behalf of the European Geosciences Union.

Abstract

The analysis is presented of the distribution of deep ocean turbulence characteristics on the horizontal scale of order 100 km in the vicinity of the Lifamatola Sill, from the Southern Maluku Sea (north of the sill) to the Seram Sea (south of the sill). The turbulence characteristics were calculated with a regional model of the Indonesian seas circulation based on the Princeton Ocean Model (POM), incorporating the Mellor-Yamada turbulence closure scheme. The analysis has been carried out for the entire Indonesian seas region, including areas around important topographic features, such as the Lifamatola Sill, the North Sangihe Ridge, the Dewakang Sill and the North and South Halmahera Sea Sills. To illustrate results of application of the Mellor-Yamada closure scheme we have focused on the description of features of turbulence characteristics across the Lifamatola Sill because dynamically this region is very important and some estimates of mixing coefficients in this area are available. As is well known, the POM model output provides both dynamical (depth-integrated and 3-D velocities, temperature, salinity, and sea-surface-height) and turbulence characteristics (kinetic energy and master scale of turbulence, mixing coefficients of momentum, temperature and salinity, etc.). As a rule, the analysis of POM modeling results has been restricted to the study of corresponding dynamical characteristics, however the study of turbulence characteristics is essential to understanding the dynamics of the ocean circulation as well. Due to the absence of direct measurements of turbulence characteristics in the analyzed area, we argued the validity of the simulated characteristics in the light of their compatibility with some general principles. Thus, along these lines, vertical profiles of across-the-sill velocities, twice the kinetic energy of turbulence, turbulence length scale, the separate terms in the equation of kinetic energy of turbulence, the Richardson number, and finally coefficients of mixing of momentum and temperature and salinity are discussed. Average values of the vertical mixing coefficient compare well with indirect estimates previously made from diagnostic calculations based on Munk's model.

OSD

9, 63–103, 2012

1 Introduction

We investigate the distribution of turbulence characteristics with horizontal scale on the order of 100 km in the deep layers of the Lifamatola Strait, calculated with a regional model of the Indonesian seas circulation. The model is based on the Princeton Ocean Model (POM), incorporating the Mellor-Yamada turbulence closure scheme. The POM is widely used in modeling the ocean circulation in various regions of the World Ocean (see http://www.aos.princeton.edu/WWWPUBLIC/htdocs.pom/ for POM details). POM model output provides both dynamical (depth-integrated and 3-D velocities, temperature, salinity, and sea-surface-height) and turbulence characteristics (kinetic energy and master scale of turbulence, mixing coefficients of momentum, temperature and salinity). As a rule, the analysis of POM modeling results concerning the 3-D circulation has been restricted to the study of the distribution of dynamical characteristics, and in a few papers only have features of turbulence characteristics been intrinsically analyzed (see, e.g., Ezer, 2000; Oey et al., 1985; Cummins, 2000; Wijesekera et al., 2003; Ezer and Mellor, 2004). We think that the study of such features is essential to understanding the dynamics of the ocean circulation as well. We found a consistent distribution of turbulence characteristics on the scale of order 100 km for the entire Indonesian seas region. To illustrate results of application of the Mellor-Yamada closure scheme, we have focused our analysis on deep ocean turbulence characteristics in the vicinity of the Lifamatola Sill, from the Southern Maluku Sea (north of the sill) to the Seram Sea (south of the sill), because dynamically this region is very important and some estimates of mixing coefficients there are available. Other regions in the Indonesian seas have been analyzed as well and results turned out to be similar; these regions include the North Sangihe Ridge, the Dewakang Sill and the sills surrounding the Halmahera Sea, specifically the north and south sills. The Lifamatola Sill is the deepest connection between the Pacific Ocean and the interior Indonesian seas, the Banda Sea and the Flores Sea, and is the main source of deep water to the Seram and Banda Seas (see, e.g., Gordon, 2005; van Aken et al., 1988, 2009; O'Driscoll and

OSD
9, 63–103, 2012

Kamenkovich, 2009). The deep flow across the Lifamatola Sill is one of the major components of the Indonesian Throughflow (ITF), which is a key element of the World Ocean thermohaline circulation system or Ocean Conveyor Belt (see, e.g., Gordon, 2005, for details).

To the best of our knowledge, there have been only a few direct measurements of turbulent characteristics in the Indonesian seas area. We can refer to the pioneering paper of Stommel and Fedorov (1967) who discovered microstructure in temperature and salinity profiles from STD recorders near Timor and Mindanao, and to detailed microstructure measurements made by Alford et al. (1999) in the Banda Sea near 100 m depth over a 2 week period. Unfortunately, these data refer to small-scale turbulence and cannot be used for the comparison with our calculations. So we can rely only on estimates of basin scale coefficients of vertical mixing in the Banda and Seram Seas, derived from diagnostic calculations by Gordon et al. (2003), van Aken et al. (1988) and van Aken et al. (1991) based on the 1-D temperature equation suggested by Munk (1966). We think that the estimate of characteristics such as q^2 (twice the kinetic energy of turbulence), ℓ (the master scale of turbulence), K_M, K_H, (coefficients of vertical mixing of momentum and temperature and salinity), Richardson number, etc., which are provided by POM along with 3-D velocity, temperature and salinity distributions is a step forward compared with the analysis of the 1-D temperature equation. At the same time, estimates obtained by Gordon and van Aken by assuming some values of basin averaged vertical velocity can be used for comparison with averaged mixing coefficients found in this paper.

We stress that mixing coefficients K_M (momentum) and K_H (temperature and salinity) were not specified apriori, but calculated within the model. Because the large-scale currents and temperature and salinity distributions have been adequately described by our model, we argue that the estimate of mixing coefficients K_M and K_H is also reasonable. Otherwise, we would not obtain an adequate description of currents and temperature-salinity distributions, because values of K_M and K_H impact directly those distributions. This conclusion is supported also by the comparison of our mixing

OSD
9, 63–103, 2012

coefficients and those estimated by Gordon et al. (2003) and van Aken et al. (1988). It is well known that K_M and K_H are proportional to q (twice the kinetic energy of turbulence) and ℓ (the master scale of turbulence), see formula (1). Therefore, the analysis of q and ℓ deserve attention as well. In our model, q is governed by Eq. (6), which we consider to be well founded. Thus, the large-scale q is shaped by the large-scale wind turbulence, shear and buoyancy production and dissipation. We think that adequacy of dynamical characteristics and mixing coefficients instill confidence in q-simulated data, although we have no observational data for direct comparison. We would like to stress that we study averaged turbulence characteristics with horizontal scale on the order of 100 km. Turbulence characteristics with smaller horizontal scales, say on the order of 100 m (for example, turbulence generated by lee waves in the vicinity of the sill), are not considered in this paper. The analysis of such motions usually requires a non-hydrostatic model, very detailed bottom topography and horizontal grid spacing on the order of 10 m (see, e.g., Xing and Davies, 2006, 2007). Equation (8), for master scale of turbulence, is a different matter. We do not think that this equation is well founded. So it is hardly surprising that the calculation of ℓ will not be completely adequate, at least in some layers. The regional model of the Indonesian seas circulation allowed us to learn a lot about the distribution of dynamical characteristics (currents, temperature and salinity) in the Indonesian seas. We think that our estimates of large scale turbulence characteristics are useful as well. Unfortunately, we have no direct arguments in support of this statement. But we also have no *direct* arguments against it. Our decision on adequacy of estimated turbulence characteristics is based also on results of the analysis of their compatibility with some general principles.

We will start with a brief description of our model and basic equations for determining turbulence characteristics (Sect. 2). Then in Sect. 3 we discuss results of the analysis of the velocity field in the area of the Lifamatola Strait, q and ℓ distributions and their shaping, Richardson number, coefficients S_M and S_H in the expression for mixing coefficients, and finally mixing coefficients K_M and K_H. Concluding remarks are outlined in Sect. 4.

OSD
9, 63–103, 2012

2 Model description

For a full model description see O'Driscoll and Kamenkovich (2009). The model domain, Fig. 1, extends throughout the Indonesian seas region and has 250×250 grid cells in the horizontal, identified in Fig. 1 by i and j. The model has horizontal resolution of ~ 10 km in both i- and j-horizontal directions, which is sufficient to resolve all major topographic features in the region. The ETOPO5 data base was used in our calculation of smoothed topography. Important localized topographic features, such as sills, were smoothed following the recommendations of the POM, such that the basic structure of the sill was retained, while the bottom slope concerning the pressure gradient problem associated with the σ-coordinate system was not an issue. The model has four open ports to simulate the impact of major currents entering and exiting the region. The orthogonal curvilinear coordinate system used in the POM has been rotated relative to the latitude-longitude system so that the open port in the Indian Ocean region (IO port) lies on the transect line extending from Java to Northwest Australia along which observations were made (see, e.g., Fieux et al., 1994; Sprintall et al., 2000). There are three open ports in the Pacific region: the Mindanao Current port in the north (MC port); the New Guinea Coastal Current port (NGCC port) just to the north of New Guinea/Irian Jaya; and the North Equatorial Counter Current port (NECC port) in the east (port locations are shown in Fig. 1). By and large, Pacific waters enter the model domain through the MC and NGCC ports and exit partially through the NECC port. Part of the Pacific waters enter the Indonesian seas area and cross through the region, before exiting the model domain in the Indian Ocean through the IO port. This is the Indonesian Throughflow (ITF). The grey (dotted) regions in Fig. 1 are shallow (depth is less than 100 m) and are considered as land. However, the depth in the grey region in the Indian Ocean in the southwestern corner of the model domain is greater than 100 m but has been excluded from the model integration to facilitate the Indian Ocean open port. There are 29 σ-levels in the vertical so that important features of the vertical structure of temperature and salinity are properly resolved over all types of topography.

OSD
9, 63–103, 2012

At the open ports, normal depth-averaged velocities are specified based on the prescribed total transport and assumed simple distributions of this velocity across the port. For the normal velocity in 3-D motion, Orlanski's condition with nudging was employed (see Marchesiello et al., 2001). Tangential velocity is zero for both the 2-D and 3-D motion. POM recommended boundary conditions are used at closed boundaries. Because of various restrictions, e.g., the NGCC crossing the equator and the grid spacing of Levitus climatology (Conkright et al., 2002), it was not possible to calculate geostrophic velocities at the open ports from available observations and climatology. Therefore, as an alternative, we used published observations and some modeling results to determine typical port normal velocities and total port transports. A detailed analysis of observational data for all ports and calculation of port normal velocities and corresponding transports was performed. It was supposed that such an approach is more reliable than the use of results from a global OGCM. For example, the area of formation of the NGCC has such a complicated coastline geometry that it is hardly possible to reasonably model the circulation in such an area with a global OGCM.

At the sea surface boundary, the Adjusted Southampton Oceanography Centre (SOC) surface flux climatology Grist and Josey (2003) is used in the calculation of surface heat flux, which is equal to the sum of long wave radiation, latent heat (evaporation) and sensible heat fluxes. Since the flux of fresh water at the surface in the Indonesian seas is very poorly known, sea surface salinity is specified from Levitus climatology Conkright et al. (2002). In the near surface and deep ocean (sub-thermocline water), a very weak nudging of T and S to climatology was introduced to account for mixing processes not correctly parameterized in the model. Monthly climatological winds are taken from the Comprehensive Ocean-Atmosphere Data Set (COADS), analyzed by da Silva et al. (1994) and are calculated at every internal time step.

Tides have not been directly included in the model. However, additional friction has been incorporated into the momentum equations as a proxy for important tidal friction in the vicinity of some passages and sills. The approach is rather crude but tides somehow needed to be taken into account. Otherwise, due to western intensification,

OSD
9, 63–103, 2012

for example, we obtained overly strong flows through certain passages and straits. A similar approach was taken by Schiller et al. (1998). The direct incorporation of tides is a separate difficult problem.

It is generally accepted now that a background diffusivity of $10^{-5}\,m^2\,s^{-1}$ is added to the coefficients of vertical mixing to represent mixing processes not modeled by the Mellor-Yamada scheme (e.g., internal waves), see, e.g., Ezer (2000).

It was shown that the developed regional model adequately describes the circulation in the Indonesian seas O'Driscoll and Kamenkovich (2009); Kamenkovich et al. (2009); Rosenfield et al. (2010). We list principal results here. First, we have shown that basic features of temperature and salinity distributions along with the current pattern with scale of order 100 km were reproduced reasonably well. We demonstrated a satisfactory agreement of simulated transports with transports observed during the INSTANT program. Second, it was proved that the pressure difference between the Pacific and Indian Ocean is not a major factor determining the total transport of the ITF. All factors influencing this total transport were revealed and their roles were clarified. Third, we managed to disclose the path of South Pacific Water entering the Indonesian seas region as a branch of the New Guinea Coastal Current. We have shown that this water flows around Halmahera island and then enters the region through the Maluku Sea and across the Lifamatole Strait.

The developed model uses the Mellor-Yamada scheme to describe turbulence characteristics. The scheme has been successsfully applied to various regions of the World Ocean. Although we did not find published results of direct comparison of turbulence characteristics simulated by the POM (incorporating the Mellor-Yamada scheme of closure) with corresponding observed characteristics, there are many results of modeling such phenomena, the structure of which depends significantly on the chosen scheme of closure. For example, Ezer (2005), studying results of modeling near the Denmark Straits bottom dense overflow came to the conclusion that the "Mellor-Yamada scheme represents the subgrid-scale mixing very well". Similarly, Ezer and Weatherly (1990), studying pools of cold water flowing on the bottom of the ocean in the High Energy

OSD
9, 63–103, 2012

Bottom Boundary Layer Experiment region in the North Atlantic, concluded that bottom turbulence and boundary-layer dynamics were simulated adequately. The POM uses Smagorinsky's scheme to parameterize sub-grid scale horizontal diffusion of momentum and scalar characteristics.

For completeness of outline, we write out the basic relations of the Mellor-Yamada turbulence closure scheme (see Mellor, 2004). Coefficients of vertical mixing of momentum, K_M, and vertical mixing of salt and temperature, K_H, are represented by

$$K_M = S_M q \ell \qquad K_H = S_H q \ell, \tag{1}$$

where q^2 is twice the kinetic energy (per unit mass) of turbulence; ℓ is a master scale of turbulence; S_M and S_H are nondimensional characteristics depending on the Richardson number, Ri,

$$\mathrm{Ri} = -\frac{\ell^2}{q^2} N^2, \tag{2}$$

where N is the local buoyancy frequency. For calculation of S_M and S_H the following empirical formulas are used

$$S_H = \frac{A_2[1 - 6(A_1/B_1)\mathrm{stf}]}{1 - [(3A_2B_2/\mathrm{stf}) + 18A_1A_2]\mathrm{Ri}} \tag{3}$$

$$S_M = \frac{A_1[1 - 3C_1 - 6(A_1/B_1)\mathrm{stf}] + (18A_1^2 + 9A_1A_2)\mathrm{Ri}}{1 - 9A_1A_2\mathrm{Ri}}. \tag{4}$$

Here, stf is a function of Ri. It is introduced to describe the effect of stratification,

$$\mathrm{stf}(\mathrm{Ri}) = \begin{cases} 1.0 & \mathrm{Ri} \geq 0 \\ 1.0 - 0.9(\mathrm{Ri}/\mathrm{Ri}_c)^{3/2} & \mathrm{Ri}_c < \mathrm{Ri} < 0 \\ 0.1 & \mathrm{Ri} \leq \mathrm{Ri}_c \end{cases} \tag{5}$$

OSD
9, 63–103, 2012

and $A_1 = 0.92$; $B_1 = 16.6$; $A_2 = 0.74$; $B_2 = 10.1$; $C_1 = 0.08$. Ri_c is the critical value of Ri, $\mathrm{Ri}_c = -6.0$.

Two equations are formulated to determine q^2 and $q^2\ell$, respectively, in x,y,σ-coordinates, $\sigma = \frac{z-\eta}{H+\eta}$, where H is the depth of the ocean and η is sea-surface-height. The q^2-equation is

$$\frac{\partial q^2 D}{\partial t} + \frac{\partial u q^2 D}{\partial x} + \frac{\partial v q^2 D}{\partial y} + \frac{\partial \omega q^2}{\partial \sigma} = \frac{\partial}{\partial \sigma}\frac{K_q}{D}\frac{\partial q^2}{\partial \sigma} + \frac{2K_M}{D}\left[\left(\frac{\partial u}{\partial \sigma}\right)^2 + \left(\frac{\partial v}{\partial \sigma}\right)^2\right] - 2DK_H N^2 - \frac{2Dq^3}{B_1 l}\mathrm{stf} + \frac{\partial}{\partial x}\left(HA_H\frac{\partial q^2}{\partial x}\right) + \frac{\partial}{\partial y}\left(HA_H\frac{\partial q^2}{\partial y}\right), \quad (6)$$

where u and v are zonal and meridional velocities, respectively; ω is the "vertical" velocity in the POM model (essentially, it is the difference between the particle velocity normal to the surface $\sigma = \mathrm{const}$, and the velocity with which the surface $\sigma = \mathrm{const}$ is moving); $D = H + \eta$; K_q is the coefficient of vertical diffusion of q^2 where $K_q = 0.41K_H$; $A_H = 0.2A_M$, where A_M is the coefficient of horizontal diffusion of momentum, calculated from Smagorinsky's formula. The first term on the rhs of Eq. (6) is the vertical diffusion; the second term is the production of turbulence kinetic energy (TKE) due to vertical shear; the third term is the work (per unit time) of buoyancy forces; the fourth term is the dissipation of TKE; and the fifth term is the horizontal diffusion of q^2.

It is useful to write out the difference form of Eq. (6). First, we integrate this equation over the grid cell with area S_g and replace these integrals with S_g multiplied by the integrand taken at the center of cell. By denoting, e.g., D at $t_n = n\Delta t$ as $D^{(n)}$, where Δt is the time step and dividing all terms of the equation on $S_\mathrm{g}D^{(n+1)}$ yields

$$\frac{\left(q^2\right)^{(n+1)} - \frac{D^{(n-1)}}{D^{(n+1)}}\left(q^2\right)^{(n-1)}}{2\Delta t} +$$

OSD
9, 63–103, 2012

$$\frac{1}{D^{(n+1)}S_g}\left([\text{sum of horizontal advective fluxes of} q^2 D] + \frac{\partial \omega q^2}{\partial \sigma} S_g\right)^{(n)} =$$

$$\frac{1}{(D^{(n+1)})^2}\frac{\partial}{\partial \sigma}\left[K_q^{(n)}\left(\frac{\partial q^2}{\partial \sigma}\right)^{(n+1)}\right] + \frac{2K_M^{(n)}}{(D^{(n+1)})^2}\left[\left(\frac{\partial u}{\partial \sigma}\right)^2 + \left(\frac{\partial v}{\partial \sigma}\right)^2\right]^{(n)} -$$

$$2K_H^{(n)}N^{2(n)} - \frac{2q^{(n-1)}}{B_1 l^{(n-1)}}\text{stf}^{(n)}(q^2)^{(n+1)} +$$

$$\frac{1}{D^{(n+1)}S_g}(\text{sum of horizontal diffusion fluxes of} q^2)^{(n-1)}. \quad (7)$$

The q^2-equation is used in many turbulence closure schemes by invoking different parameterizations of diffusion, production and dissipation of turbulence energy. The $q^2\ell$-equation is utilized in the Mellor-Yamada scheme only (see a discussion in Burchard, 2001). This equation is as follows

$$\frac{\partial q^2 \ell D}{\partial t} + \frac{\partial u q^2 \ell D}{\partial x} + \frac{\partial v q^2 \ell D}{\partial y} + \frac{\partial \omega q^2 \ell}{\partial \sigma} = \frac{\partial}{\partial \sigma}\frac{K_q}{D}\frac{\partial q^2 \ell}{\partial \sigma} + E_1 \ell \frac{K_M}{D}\left[\left(\frac{\partial u}{\partial \sigma}\right)^2 + \left(\frac{\partial v}{\partial \sigma}\right)^2\right]$$

$$- E_1 D \ell K_H N^2 - \frac{Dq^3}{B_1} W \text{stf} + \frac{\partial}{\partial x}\left(HA_H \frac{\partial q^2 \ell}{\partial x}\right) + \frac{\partial}{\partial y}\left(HA_H \frac{\partial q^2 \ell}{\partial y}\right) \quad (8)$$

where $E_1 = 1.8$; $E_2 = 1.33$ and W is the so-called wall proximity function,

$$W = 1 + E_2\left[\frac{\ell}{\kappa}(|z-\eta|^{-1} + |z+H|^{-1})\right]^2, \quad (9)$$

and κ is von Karman's constant. The physical meaning of the separate terms on the rhs of Eq. (8) is the same as the corresponding terms of Eq. (6). The difference form

OSD
9, 63–103, 2012

of Eq. (8) is as follows,

$$\frac{\left(q^2\ell\right)^{(n+1)} - \frac{D^{(n-1)}}{D^{(n+1)}}\left(q^2\ell\right)^{(n-1)}}{2\Delta t} +$$

$$\frac{1}{D^{(n+1)}S_g}\left([\text{sum of horizontal advective fluxes of } q^2\ell D] + \frac{\partial \omega q^2\ell}{\partial\sigma}S_g\right)^{(n)} =$$

$$\frac{1}{(D^{(n+1)})^2}\frac{\partial}{\partial\sigma}\left[K_q^{(n)}\left(\frac{\partial q^2\ell}{\partial\sigma}\right)^{(n+1)}\right] + E_1\ell^{(n)}\frac{K_M^{(n)}}{(D^{(n+1)})^2}\left[\left(\frac{\partial u}{\partial\sigma}\right)^2 + \left(\frac{\partial v}{\partial\sigma}\right)^2\right]^{(n)} -$$

$$E_1\ell^{(n)}K_H^{(n)}N^{2(n)} - \frac{q^{(n-1)}}{B_1\ell^{(n-1)}}W^{(n)}\text{stf}^{(n)}(q^2\ell)^{(n+1)} +$$

$$\frac{1}{D^{(n+1)}S_g}(\text{sum of horizontal diffusion fluxes of } q^2\ell)^{(n-1)}. \quad (10)$$

The vertical boundary conditions for q^2 and $q^2\ell$ at the surface are, respectively,

$$q^2 = B_1^{2/3}\sqrt{\left(\frac{\tau_x}{\rho_0}\right)^2 + \left(\frac{\tau_y}{\rho_0}\right)^2}; \quad q^2\ell = 0 \quad \text{at} \quad z = 0; \quad (11)$$

where τ_x and τ_y are the components of the wind stress and ρ_0 is the mean density. The corresponding boundary conditions at the bottom are

$$q^2 = B_1^{2/3}C_z^2(u^2 + v^2); \quad q^2\ell = 0 \quad \text{at} \quad z = -H; \quad (12)$$

where C_z is the so-called drag coefficient, calculated in the model by using the so-called law of the wall. The horizontal boundary conditions are

$$q^2 = \varepsilon; \quad q^2\ell = \varepsilon \quad \text{at horizontal boundaries}, \quad (13)$$

where ε has been set to 10^{-10}.

OSD
9, 63–103, 2012

3 Results and analysis

Model simulated deep water transports across the sill below 1200 m are in good agreement with those given by van Aken et al. (1988) who calculated a deep southward transport of ∼1.5 Sv from a current mooring deployed between January and March 1985, while model deep southward transport is approximately 1.4 Sv in February Kamenkovich et al. (2009). In the same paper, van Aken et al. (1988) estimated an annual deep transport of the order of 1 Sv in good agreement with the model (see Kamenkovich et al., 2009). But later on van Aken et al. (2009) calculated a long-term mean deep transport of 2.4–2.5 Sv for 34 months between 2004 and 2006 from a mooring containing current meters and ADCPs at the sill as part of the INSTANT program (see Sprintall et al., 2004). van Aken et al. (2009) state that the reduced transport estimated in van Aken et al. (1988) is due partly to the shorter observation period and partly to the smaller thickness of the overflow layer estimated from linear extrapolation. The simulated structure of velocity profile is in very good agreement with that observed by van Aken et al. (1988). All models have some tuning parameters to make compatible some separate values. Therefore we argue that the comparison of structures of velocity profiles is more important than that of some separate values. Figure 2 is a vertical section of v-velocities through the Lifamatola Sill, and shows a southward flow extending from below 1200 m to the bottom through the sill. At the sill, southward velocities increase with depth to a maximum value of over 0.15 m s^{-1} at ∼1700 m. Model velocities across the sill are in very good agreement with those of Broecker et al. (1986) who found mean velocities of ∼20 cm s^{-1} just above the sill over a 28 day period in August–September 1976. However, they are less than those measured by van Aken et al. (1988) who found mean velocities of 61 cm s^{-1} at 60 m above the bottom in January–March 1985, and van Aken et al. (2009) who found maximum velocities of 65 cm s^{-1} at ∼70 m above the bottom. Simulated v-velocities are also southward below sill depth, north and south of the sill, to a depth of ∼2400 m. Velocity is northward below ∼2400 m both north and south of the sill. A weak northward

OSD
9, 63–103, 2012

current is seen to extend from 1200 m into the thermocline across the entire section. Note that all model results presented are from the 15 August after 15 yr of model run.

v-velocity profiles through the sill below 1200 m are shown in detail in Fig. 3. It is seen that the southward current at the sill, middle (3rd) profile, • extends from 1300 m to the bottom and maximum velocity is seen at about 1700 m or deeper, below which velocity rapidly decreases. The observed mean profile shows southward flow across the sill at 129° clockwise from north and into the Seram Sea. This practically coincides with the y-component of model flow across the sill, since the model domain is rotated anti-clockwise relative to north-south, see Fig. 1. The profile to the south of the sill (4th profile, ∘) is similar to that at the sill but the southward current is deeper because of the greater depth, and reaches a greater maximum velocity of almost 0.20 m s^{-1} just above the bottom. Moving into deeper water, both south and north, the southward (negative) current is not as strong as at the sill but extends to deeper than 2000 m in all cases. Currents are strongly northward (positive) below ∼2400 m at the deepest profiles (1st and 5th profiles), extending through the lower 200–300 m of the water column. Note also the rapid change of velocity (decrease in magnitude) just above the bottom in all profiles which is due to the bottom boundary condition used in the POM,

$$K_m \frac{\partial v}{\partial z} = C_z (u^2 + v^2)^{1/2} v \quad \text{at} \quad z = -H. \tag{14}$$

From Eq. (14) it follows that if $v(-H) > 0$ then $\frac{\partial v}{\partial z}(-H) > 0$ (1st and 5th profiles); if $v(-H) < 0$ then $\frac{\partial v}{\partial z}(-H) < 0$ (3rd and 4th profiles). In the case of the 2nd profile $v(-H)$ is close to zero. This rapid change in velocity is present in the observed profile (see Fig. 3), which suggests that the bottom boundary condition Eq. (14) is quite adequate.

We analyzed vertical profiles of turbulence characteristics at five locations across the sill. Profiles of q^2, twice the TKE, are shown in Fig. 4. At the sill (• 3rd profile), large values of q^2 are confined to the very bottom of the water column, above which values are rapidly reduced and are set to the model background value of 10^{-9} m^2 s^{-2}.

OSD
9, 63–103, 2012

A similar profile is seen to the south of the sill (∘ 4th profile). This feature is also seen in the other three profiles. However, in addition, at these three profiles, 1st, 2nd, 5th, large values of q^2 extend upward for several hundred metres above the bottom; between 1900–2600 m in the 1st profile (+); 1900–2100 m in the 2nd profile (□); and 2000–2500 m in the 5th profile (×). Above this layer q^2 are also small and are set to the model background value. The increase in q^2 above the bottom (profiles 1, 2, and 5) is reasonable because the intensity of turbulence should first increase, as one moves downwards and then decrease at the very bottom. However, due to the increase of velocity shear at the very bottom and ensuing shear production of q^2, the pronounced increase in q^2 values occur near the very bottom (see Table 1).

Profiles of $q^2\ell$ are shown in Fig. 5. Immediately clear is the similarity with q^2 profiles (Fig. 4), except close to the bottom boundary. The analogous structures of Eqs. (7) and (10) explain this similarity, while the difference in bottom boundary conditions, Eq. (12), explains the additional rapid change (decrease) of $q^2\ell$ near the bottom. Yet, the real question is whether the distribution of ℓ that is determined by distributions of q^2 and $q^2\ell$ is reasonable (see Fig. 6).

How are q^2 and $q^2 l$ generated? To answer this question, we estimated separately all terms in Eqs. (7) and (10) to reveal the leading terms (see Tables 1 and 2). It is worth noting that these tables are calculated only for those σ-levels for which q^2 and $q^2 l$ are greater than 10^{-9}, the point being that if q^2 and $q^2 l$ calculated from Eqs. (7) and (10) are less than this value, the POM replaces them with 10^{-9} in the SI system. Therefore, the analysis of contributions of different terms in Eqs. (7) and (10) at these levels is meaningless. Tables 1 and 2 give estimates of the separate terms in Eqs. (7) and (10) at the same 5 profiles across the sill from the bottom, $\sigma(kb)$, where $kb = 29$, up to a depth of 0.8 times water column depth, $\sigma(kb-6)$. Recalling that values of σ range from 0 at the surface to −1 at the ocean bottom, we chose the following σ-values: $\sigma(kb-6) = -0.80$; $\sigma(kb-5) = -0.88$; $\sigma(kb-4) = -0.94$; $\sigma(kb-3) = -0.9922$; $\sigma(kb-2) = -0.9961$; $\sigma(kb-1) = -0.9994$. The relatively large number of σ-levels close to the bottom allows for a reasonable description of a bottom boundary layer.

OSD
9, 63–103, 2012

Table 1 shows that at all 5 profiles except the 2nd, shear production of q^2 and its dissipation are leading factors at levels very close to the bottom (due to increased velocity gradient at these levels, see Fig. 3). At other levels, such a balance of terms in Eq. (7) is not observed. There are levels and profiles at which any and all terms in Eq. (7) can be important. Nevertheless, it is worth noting that the vertical diffusion of q^2 is important at one level of the 2nd, 4th and 5th profiles only, while horizontal diffusion is important at more levels (especially profiles 1 and 2). Buoyancy production of q^2 is basically unimportant at profile 1 only.

It is appropriate to discuss now profiles of shear production (Fig. 7), buoyancy production (Fig. 8) and dissipation of q^2 (Fig. 9). For shear production, we see first that values increase as one moves downwards towards the bottom, then decrease above the bottom, before finally increasing substantially very close to the bottom (except profile 2), which is certainly due to the increase in velocity shear close to the bottom (Fig. 3). Notice that velocity shear is small at profile 2. Note also in Fig. 3, there is very little shear just above the bottom points, particularly in profiles 1 and 2. This lack of shear combined with the little or no shear at these depths in the u-component of velocity (not shown) explains the reduction in shear production here. Buoyancy production is the product of buoyancy frequency, N^2, with the mixing coefficient, K_H, (Eq. 6). Values decrease gradually from 1200 m down through the water column. However, there is an increase in values of profiles 1 (between 2100–2500 m), 2 (between 1900–2100), 4 (between 1700–1900 m), and 5 (between 2000–2400). Values for all profiles increase rapidly just above the the bottom (see discussion of Fig. 10). In the region of gradually decreasing values, buoyancy frequency also decreases gradually (Fig. 10) while K_H is essentially constant (Fig. 13). The increase in buoyancy production above the bottom in profiles 1, 2, and 5 is due to the increase in q^2 and the subsequent increase in K_H, while the increase in profile 4 is due to the increase in N^2. The increase in magnitude of dissipation close to the bottom is due to the combined effect of increased q^2 with decreased ℓ, while the increase just above this is due to the combined effect of decreased q^2 with increased ℓ.

OSD
9, 63–103, 2012

The features exposed in Table 1 are also seen in Table 2 (due to the similarity of Eqs. 7 and 10). Consider now profiles of the turbulence length scale ℓ. From a general standpoint, we should expect to see constant values in the main depth of the ocean, with a gradual decrease as one moves toward the bottom. In fact, in Fig. 6, constant values are seen at all profiles in the main depth of the ocean, away from the effect of bottom topography, but the structure of ℓ at profiles 1,2 and 5 is unreasonably complicated when one moves toward the bottom. It is difficult to find any physical arguments to explain the rapid increase of ℓ below the decrease seen in these profiles. We can ascribe this behavior to the rather complicated structure of $q^2\ell$ in these profiles provided by Eq. (10), which is also difficult to explain with physical arguments. We think that the procedure for calculation of ℓ suggested by the POM does not provide the adequate behavior of ℓ within the bottom boundary layer. But taking into account the adequate reproduction of dynamical characteristics, we argue that some inconsistencies in the calculation of ℓ and connected with ℓ characteristics, e.g., the Richardson number, etc., do not influence the dynamic characteristics substantially.

Turning to the discussion of profiles of magnitude of buoyancy frequency squared, N^2 (Fig. 10), it is seen that values decrease slowly as we move down below 1200 m, as expected in the open ocean. However, profile 1 shows values increasing notably between 2300 and 2600 m. This is due to strengthening stratification there, as shown in O'Driscoll and Kamenkovich (2009) (Fig. 13, profile C and Fig. 24 $\theta - S$ diagram) and as previously observed by van Aken et al. (1988) (Fig. 7. $\theta - S$ diagram). Rapid changes of N^2 close to the bottom are probably due to some drawbacks of the POM algorithm of calculation of N^2 in the deep ocean.

Consider the profiles of the modulus of the Richardson number |Ri| (see Eq. 2) given in Fig. 11. Again we observe some rapid changes close to the bottom. In profiles 1 and 5, the rapid increase just above the bottom followed by a rapid decrease is due to the combination of rapidly increasing and decreasing ℓ with rapidly decreasing and increasing q^2, respectively, and is also seen in profile 2 to a lesser extent. Finally, profiles of mixing coefficients K_M and K_H are provided in Figs. 12 and 13, respectively, (see

OSD
9, 63–103, 2012

formulas 1). At the very bottom, $\ell = 0$, due to the model bottom boundary condition, and K_M and K_H have model background values only. Above the bottom, K_M and K_H are large for a very thin layer because q, S_M and S_H are large, and ℓ is non-zero. Above this again, K_M and K_H are briefly small in the two deepest profiles, which is explained by small values of q and S_M and S_H. We plot S_M and S_H in Figs. 14 and 15, respectively, (see formulas 3 and 4) for completion. Using the diagnostic method of Munk (1966), Gordon et al. (2003) calculated an average deep water K_M of $13.3 \times 10^{-4}\,m^2\,s^{-1}$ from temperature profiles for the Banda and Seram Seas, while van Aken et al. (1988) calculated a value of $9.0 \times 10^{-4}\,m^2\,s^{-1}$ for the deep Banda Sea system. We calculate an average K_M value of 15 to 20 $\times$ $10^{-4}\,m^2\,s^{-1}$ for deep water in the vicinity of the Lifamatola Sill. The somewhat increased values can be explained by the presence of complicated topography there. We remind th reader that in the main depth of the ocean below the thermocline vertical mixing is small and a background value of $10^{-5}\,m^2\,s^{-1}$ for K_M and K_H is generally accepted.

4 Summary and concluding remarks

The distribution of turbulence characteristics in the Indonesian seas region on the horizontal scale of order 100 km, calculated with a regional model have been investigated. The model is based on the Princeton Ocean Model (POM), incorporating the Mellor-Yamada turbulence closure scheme. By and large, the analysis of POM modeling results has generally been restricted to the distribution of dynamical characteristics. We think the study of consistent turbulence characteristics is also essential to understanding of the ocean dynamics. The analysis has been carried out for the entire Indonesian seas region, including areas around the Lifamatola Sill, the North Sangihe Ridge, the Dewakang Sill and the North and South Halmahera Sea Sills. To illustrate results of application of the Mellor-Yamada closure scheme we have focused on the description of features of turbulence characteristics in the vicinity of the Lifamatola Sill because this region is, first, very important dynamically, being the deepest connection between the Pacific Ocean and the interior Indonesian seas, and, second, because some estimates

OSD
9, 63–103, 2012

of mixing coefficients exist there (see Gordon et al., 2003; van Aken et al., 1988. The results of the analysis in other regions of the Indonesian seas turned out to be similar. As shown in several papers the incorporation in the POM of the Mellor-Yamada closure scheme gives a reasonable description of turbulence characteristics of the same scale as dynamical characteristics, see, for example, Ezer (2000).

In our model, the large-scale distribution of the turbulence kinetic energy is shaped by the large-scale wind turbulence, shear and buoyancy production and dissipation. We think that adequacy of dynamical characteristics provided by the regional model instill confidence in validity of simulated turbulence characteristics. Unfortunately, we have no observational data for *direct* comparison. We would like to stress that we study averaged turbulence characteristics with horizontal scale on the order of 100 km. Turbulence characteristics with smaller horizontal scales, say on the order of 100 m (for example, turbulence generated by lee waves in the vicinity of the sill), are not considered in this paper. The regional model of the Indonesian seas circulation allowed us to learn a lot about the distribution of dynamical characteristics (currents, temperature and salinity) in the Indonesian seas. We think that our estimates of large scale turbulence characteristics are useful as well. In addition to the comparison with diagnostic estimates of mixing coefficients by Gordon et al. (2003), (van Aken et al., 1988, 1991), our conclusion on adequacy of estimated turbulence characteristics is based also on results of the analysis of their compatibility with some general principles.

The model extends throughout the entire Indonesian seas region. There are 250 × 250 grid cells in the horizontal with resolution of ∼ 10 km and 29 σ-levels in the vertical. All major topographic features in the region are resolved. The model has four open ports to simulate the impact of major currents entering and exiting the region; 3 in the Pacific for the Mindanao Current, New Guinea Coastal Current and North Equatorial Counter Current, respectively, and 1 in the Indian Ocean through which the ITF exits the model domain. POM recommended boundary conditions are used at closed boundaries. At the surface, heat flux is calculated from surface flux climatology and wind stress is calculated from monthly climatological winds. The developed regional

OSD
9, 63–103, 2012

model has been shown to adequately model the circulation in the Indonesian seas.

Model simulated deep water transports across the sill are in good agreement with those estimated by van Aken et al. (1988) but are somewhat less than those estimated by van Aken et al. (2009). Simulated velocities show a southward flow extending from below 1200 m to the bottom through the sill. The structure of the simulated velocity profile at the sill is in very good agreement with that observed by van Aken et al. (2009), which shows a southward flow extending from below 1200 m to the bottom. We argue that the comparison of structures of velocity profiles is more important than that of separate values. Southward velocities increase with depth to a maximum value of over $0.15\,\mathrm{m\,s^{-1}}$ at ~ 1700 m. Model velocities across the sill are in very good agreement with those of Broecker et al. (1986) but are less than those measured by van Aken et al. (1988), van Aken et al. (2009). Moving away from the sill and into deeper waters both north and south, these southward currents extend to a depth of almost 2400 m below which strong simulated current reversals are seen in both the Southern Maluku and Seram Seas. A notable rapid change in velocity magnitude near the bottom is seen in all profiles due to the POM bottom boundary condition.

The structure of q^2, twice the TKE, shows that to the north of the Lifamatola Sill (in the Maluku Sea) and to the south of the sill (in the Seram Sea) large values of q^2 occur in the deep layer extending several hundred meters above the bottom. Above this layer, q^2 values are small and are set to the model background value. This increase in q^2 above the bottom is reasonable because the intensity of turbulence should first increase when one moves downwards and then decrease at the very bottom. However, the pronounced increase of q^2 as seen near the very bottom is probably due to the increase of velocity shear and the corresponding shear production of q^2 very close to the bottom. Thus, we conclude that q^2 is quite adequately reproduced by the model considered. The similarity in the structure of $q^2\ell$ and q^2, where ℓ is the turbulence length scale, is due to the similarity of their respective equations, while the difference in bottom boundary conditions explains the additional rapid change (decrease) of $q^2\ell$ near the bottom.

OSD
9, 63–103, 2012

Since the turbulence length scale, ℓ, in the Mellor-Yamada closure scheme is calculated from the solutions to both the q^2- and $q^2\ell$-equations, we estimated all terms in these equations separately to reveal whether ℓ is reasonably distributed. This was done at levels where values of q^2 and $q^2\ell$ were greater than a meaningful threshold value. In 4 of the 5 profiles analyzed, a balance exists between shear production of q^2 and its dissipation close to the bottom due to increased velocity gradient. Notably, there are σ-levels and profiles at which any and all terms can be important, vertical diffusion is important at one σ-level only, while horizontal diffusion is important at more levels, and buoyancy production is unimportant at 1 profile only. The same features are seen for the $q^2\ell$ profiles.

Shear production values increase as one moves towards the bottom, decrease above the bottom due to a reduction in shear, before increasing rapidly just above the bottom due to increased shear. Buoyancy production values decrease gradually as one moves down through the water column. Away from the sill, in deeper water, increased values are seen for a depth of several hundred meters above the bottom, due to an increase in the mixing coefficient, K_H, before decreasing again as the bottom is approached.

For turbulence length scale, ℓ, constant values are seen in the main depth of the ocean which rapidly decrease close to the bottom, as one would expect. However, in deep profiles away from the sill, the effect of topography results in the structure being unreasonably complicated as one moves towards the bottom. Since it is difficult to find any physical arguments to explain this rapid increase of ℓ, we doubt that ℓ is reproduced near the bottom adequately by the model considered. Nevertheless, this inconsistency does not influence the dynamical characteristics substantially.

Values of buoyancy frequency squared, N^2, decrease slowly as we move down through the water column. However, increasing values are seen below 2300 m to the north of the sill due to strengthening stratification in the Maluku Sea. Rapid changes of N^2 close to the bottom are probably due to some drawbacks in the POM calculation algorithm of N^2 in the deep ocean. Profiles of the modulus of Richardson number,

OSD
9, 63–103, 2012

|Ri|, also show rapid changes close to the bottom. These changes are reflected in the changes seen in profiles of K_M, K_H, S_M, and S_H. An average K_M value of 15 to 20×10^{-4} m^2 s^{-1} is calculated for deep water in the vicinity of the Lifamatola Sill. This value is a little higher than indirect estimates made previously from observations for the Banda Sea system, but it should be a reasonable estimate given the steep topography around the sill.

Acknowledgements. K. O'Driscoll would like to thank the Naval Oceanographic Office for supporting his graduate education. V. Kamenkovich gratefully acknowledges support from the National Science Foundation through grants OCE 96-33470 and OCE 01-18200.

References

van Aken, H. M., Punjanan, J., and Saimima, S.: Physical aspects of the flushing of the East Indonesian basins, Neth. J. Sea Res., 22, 315–339, 1988. 65, 66, 67, 75, 79, 80, 81, 82

van Aken, H. M., Bennekom, A. J. V., Mook, W. G., and Postma, H.: Application of Munk's abyssal recipes to tracer distributions in the deep waters of the Southern Banda basin, Oceanol. Acta, 14, 151–162, 1991. 66, 81

van Aken, H. M., Brodjonegoro, I. S., and Jaya, I.: The deep-water motion through the Lifamatola Passage and its contribution to the Indonesian throughflow, Deep-Sea Res. Pt. I, 56, 1203–1216, 2009. 65, 75, 82

Alford, M., Gregg, M., and Ilyas, M.: Diapycnal mixing in the Banda Sea: results of the first microstructure measurements in the Indonesian throughflow, Geophys. Res. Lett., 26, 2741–2744, 1999. 66

Broecker, W. S., Patzert, W. C., Toggweiler, J. R., and Stuiver, M.: Hydrography, chemistry, and radioisotopes in the southeast Asian waters, J. Geophys. Res., 91, 14345–14354, 1986. 75, 82

Burchard, H.: On the $q^2\ell$ equation by Mellor and Yamada (1982), J. Phys. Oceanogr., 31, 1377–1387, 2001. 73

Conkright, M. E., Locarnini, R. A., Garcia, H. E., O'Brien, T. D., Boyer, T. P., Stephens, C., and Antonov, J.: World Ocean Atlas 2001: Objective Analyses, Data Statistics, and Figures, Cd-rom documentation, National Oceanographic Data Center, Silver Spring, MD, 2002. 69

OSD
9, 63–103, 2012

Cummins, P.: Stratified flow over topography: time-dependent comparisons between model solutions and observations, Dynam. Atmos. Oceans, 33, 43–72, 2000. 65
Ezer, T.: On the seasonal mixed layer simulated by a basin-scale ocean model and the Mellor-Yamada turbulence scheme, J. Geophys. Res., 105, 16843–16855, 2000. 65, 70, 81
Ezer, T.: Entrainment, diapycnal mixing and transport in three-dimensional bottom gravity current simulations using the Mellor-Yamada turbulence scheme, Ocean Model., 9, 151–168, 2005. 70
Ezer, T. and Mellor, G.: A generalized coordinate ocean model and a comparison of the bottom boundary layer dynamics in terrain-following and z-level grids, Ocean Model., 6, 379–403, 2004. 65
Ezer, T. and Weatherly, G. L.: A numerical study of the interaction between a deep cold jet and the bottom boundary layer of the ocean, J. Phys. Oceanogr., 20, 801–816, 1990. 70
Fieux, M., Andrie, C., Delecluse, P., Ilahude, A. G., Kartavtseff, A., Mantisi, F., Molcard, R., and Swallow, J. C.: Measurements within the Pacific-Indian oceans throughflow region, Deep-Sea Res. Pt. I, 41, 1091–1130, 1994. 68
Gordon, A. L.: Oceanography of the Indonesian seas and their throughflow, Oceanography, 18, 14–27, 2005. 65, 66
Gordon, A. L., Giulivi, C. F., and Ilahude, A. G.: Deep topographic barriers within the Indonesian seas, Deep-Sea Res. Pt. II, 50, 2205–2228, 2003. 66, 67, 80, 81
Grist, J. P. and Josey, S. A.: Inverse analysis adjustment of the SOC air-sea flux climatology using ocean heat transport constraints, J. Climate, 20, 3274–3295, 2003. 69
Kamenkovich, V. M., O'Driscoll, K. T. A., and Nechaev, D.: Dynamics of the Indonesian seas, Part II – The role of pressure head, J. Mar. Res., 67, 159–184, 2009. 70, 75
Marchesiello, P., McWilliams, J. M., and Shchepetkin, A.: Open boundary conditions for long-term integration of regional oceanic models, Ocean Model., 3, 1–20, 2001. 69
Mellor, G. L.: Users Giude for a three-dimensional, primitive equation, numerical ocean model, Tech. rep., Program in Atmospheric and Oceanic Sciences, Princeton University, 2004. 71
Munk, W. H.: Abyssal recipes, Deep-Sea Res., 13, 707–730, 1966. 66, 80
O'Driscoll, K. T. A. and Kamenkovich, V. M.: Dynamics of the Indonesian seas circulation, Part I – The influence of bottom topography on temperature and salinity distributions, J. Mar. Res., 67, 119–157, 2009. 65, 68, 70, 79
Oey, L. Y., Mellor, G. L., and Hires, R. I.: A three-dimensional simulation of the Hudson-Raritan estuary, Part I: Description of the model and model simulations, J. Phys. Oceanogr., 15,

OSD
9, 63–103, 2012

1676–1692, 1985. 65
Rosenfield, D., Kamenkovich, V., O'Driscoll, K., and Sprintall, J.: Validation of a regional Indonesian seas model based on a comparison between model and INSTANT transports, Dynam. Atmos. Oceans, 50, 313–330, 2010. 70
Schiller, A., Godfrey, J. S., McIntosh, P. C., Meyers, G., and Wijffels, S. E.: Seasonal near-surface dynamics and thermodynamics of the Indian ocean and Indonesian throughflow in a global ocean general circulation model, J. Phys. Oceanogr., 28, 2288–2312, 1998. 70
da Silva, A. M., Young, C. C., and Levitus, S.: Atlas of Surface Marine Data 1994, Volume 2: Anomalies of Directly Observed Quantities, NOAA Atlas NESDIS 7, U.S. Department of Commerce, NOAA, NESDIS, 1994. 69
Sprintall, J., Gordon, A., Molcard, R., Ilahude, G., Bray, N., Chereskin, T., Cresswell, G., Feng, M., Ffield, A., Fieux, M., Hautala, S., Luick, J., Meyers, G., Potemra, J., Susanto, D., and Wijffels, S.: The Indonesian throughflow: past, present and future monitoring. in: Proceedings from the Sustained Observations for Climate of the Indian Ocean Workshop, Perth, Australia, Technical report, IOC/CLIVAR, 2000. 68
Sprintall, J., Wijffels, S., Gordon, A. L., Ffield, A., Molcard, R., Susanto, R. D., Soesilo, I., Sopaheluwakan, J., Surachman, Y., van Aken, H. M.: A New International Array to Measure the Indonesian Throughflow: INSTANT, EOS Transactions, 85:39, 369–376, 2004. 75
Stommel, H. and Fedorov, K. N.: Small scale structure in temperature and salinity near Timor and Mindanao, Tellus, 19, 306–324, 1967. 66
Wijesekera, H. W., Allen, J. S., and Newberger, P. A.: Modeling study of turbulent mixing over the continental shelf: comparison of turbulent closure schemes, J. Geophys. Res., 108, 1–25, doi:10.1029/2001JC001234, 2003. 65
Xing, J. and Davies, A. M.: Influence of stratification and topography upon internal wave spectra in the region of sills, Geophys. Res. Lett., 33, 1–5, doi:10.1029/2006GL028092, 2006. 67
Xing, J. and Davies, A. M.: On the importance of non-hydrostatic processes in determining tidally induced mixing in sill regions, Cont. Shelf Res., 27, 2162–2185, 2007. 67

OSD
9, 63–103, 2012

Table 1. Near bottom values of different terms of the q^2 equation at 5 points (location indices are given) across the Lifamatola Sill as follows: rate of time difference (td), 3-D advection (ad), shear production (sp), work of buoyancy forces (bp), dissipation (dp), vertical diffusion (vd), and horizontal diffusion (hd) and the difference between the lhs and rhs of Eq. (7) (resid), resid = td + ad – (vd + sp + bp + dp + hd). Leading terms are indicated by bold. All units in $m^2 s^{-3}$.

σ	td	ad	sp	bp	dp	vd	hd	resid
	(a)	$i = 138$	$j = 154$					
$\sigma(kb-6)$	**−9.0e−11**	**2.9e−11**	2.6e−13	**−1.8e−11**	**−1.6e−11**	2.5e−13	**−2.7e−11**	−1.4e−15
$\sigma(kb-5)$	**−2.0e−10**	−3.7e−12	**1.8e−10**	**−7.2e−11**	**−3.1e−10**	2.9e−12	**−1.1e−11**	9.5e−16
$\sigma(kb-4)$	**−6.3e−10**	**−3.6e−10**	**3.8e−10**	**−3.2e−10**	**−1.5e−9**	−7.3e−12	**4.7e−10**	−3.7e−15
$\sigma(kb-3)$	**2.2e−10**	5.0e−11	1.4e-12	−8.0e−12	-4.4e-16	6.4e−12	**2.7e−10**	6.7e−17
$\sigma(kb-2)$	**6.7e−10**	**−4.3e−10**	5.4e−13	-2.8e-11	−1.3e−15	6.9e-11	**1.9e−10**	−5.4e−17
$\sigma(kb-1)$	5.1e−10	-3.8e-10	**2.9e−8**	−3.4e−10	**−3.1e−8**	1.8e−9	9.2e-11	2.1e−15
	(b)	$i = 138$	$j = 152$					
$\sigma(kb-4)$	**−1.5e−10**	**2.4e−10**	2.7e−11	**−1.1e−10**	**−1.3e−10**	−2.9e−13	**3.1e−10**	−5.7e−15
$\sigma(kb-3)$	**−3.6e−11**	**1.1e−10**	1.4e−11	-4.8e-11	−4.3e−11	-7.4e-13	**1.5e−10**	−1.2e−14
$\sigma(kb-1)$	1.8e−12	**1.1e−10**	8.3e−12	**−9.0e−11**	−6.8e−18	**7.8e−11**	**1.2e−10**	−1.8e−13
	(c)	$i = 138$	$j = 150$					
$\sigma(kb-1)$	5.4e−9	1.3e-9	**3.2e−7**	−1.2e−9	**−3.2e−7**	4.6e−9	6.7e-11	−8.0e−12
	(d)	$i = 138$	$j = 148$					
$\sigma(kb-2)$	1.6e−10	2.5e-10	**2.1e−9**	**−1.6e−9**	**−4.0e−9**	**3.6e−9**	3.1e−10	−6.5e−14
$\sigma(kb-1)$	7.3e−9	1.0e-9	**1.5e−6**	−9.8e−10	**−1.5e−6**	−7.6e−10	-1.6e-10	1.6e−13
	(e)	$i = 138$	$j = 146$					
$\sigma(kb-6)$	**5.5e−11**	**−9.4e−11**	1.3e−13	**−5.2e−11**	−1.2e−16	5.1e-14	**1.1e−11**	−5.6e−17
$\sigma(kb-5)$	−2.0e−12	**−2.4e−10**	1.2e−11	**−1.0e−10**	−9.3e−11	6.9e-14	−6.2e−11	1.8e−15
$\sigma(kb-4)$	−7.5e−11	6.1e-11	**5.4e−10**	**−1.8e−10**	**−3.0e−10**	−5.4e−13	-7.9e-11	−1.5e−15
$\sigma(kb-2)$	5.8e−11	**−4.4e−10**	**1.7e−9**	**−2.0e−10**	**−2.0e−9**	**−1.7e−10**	**2.5e−10**	−4.9e−12
$\sigma(kb-1)$	1.0e−13	-1.4e-10	**2.1e−9**	−5.6e−12	**−2.7e−9**	2.0e−10	2.7e-10	−3.3e−16

OSD
9, 63–103, 2012

Table 2. Same as Table 1 but for $q^2\ell$.

σ	td	ad	sp	bp	dp	vd	hd	resid
	(a)	$i = 138$	$j = 154$					
$\sigma(kb-6)$	**−4.6e−9**	**3.6e−9**	1.7e−11	**−1.2e−9**	−7.4e−10	1.1e-11	**−1.8e−9**	−8.7e−15
$\sigma(kb-5)$	**−9.6e−9**	**4.9e−9**	**1.1e−8**	**−4.2e−9**	**−1.4e−8**	8.7e−11	-5.8e-10	−1.7e−13
$\sigma(kb-4)$	**−2.2e−8**	−1.1e−8	**1.6e−8**	**−1.3e−8**	**−6.0e−8**	−2.7e−10	**1.9e−8**	−8.9e−13
$\sigma(kb-1)$	−5.8e−11	-2.8e-10	**1.2e−8**	−1.4e−10	**−1.2e−8**	−3.8e−10	9.6e-11	−2.1e−11
	(b)	$i = 138$	$j = 152$					
$\sigma(kb-4)$	**−3.5e−9**	**1.0e−8**	**1.1e−9**	**−4.0e−9**	**−5.4e−9**	−1.4e−11	**1.3e−8**	−1.7e−14
$\sigma(kb-3)$	−3.2e−11	-6.7e-10	1.9e−10	-6.5e-10	**−2.2e−9**	−8.0e−13	**1.8e−9**	−2.8e−12
	(c)	$i = 138$	$j = 150$					
$\sigma(kb-1)$	9.2e−10	4.3e-10	**1.2e−8**	−3.3e−10	**−8.1e−8**	−2.9e−9	3.0e-11	−1.6e−9
	(d)	$i = 138$	$j = 148$					
$\sigma(kb-2)$	2.1e−11	**7.5e−10**	**1.3e−9**	**−9.9e−10**	**−1.5e−9**	**1.2e−9**	**7.1e−10**	−9.8e−12
$\sigma(kb-1)$	1.5e−9	3.9e-10	**4.8e−7**	−3.1e−10	**−4.5e−7**	−1.5e−8	-4.1e-11	−2.7e−11
	(e)	$i = 138$	$j = 146$					
$\sigma(kb-5)$	**2.1e−9**	**−9.7e−9**	5.4e−10	**−4.4e−9**	**−2.9e−9**	1.7e−12	**−2.9e−9**	−6.0e−14
$\sigma(kb-4)$	2.0e−10	**3.3e−9**	**2.1e−8**	**−6.7e−9**	**−1.1e−8**	−2.2e−11	**−2.8e−9**	−7.5e−14
$\sigma(kb-2)$	1.4e−10	**−1.3e−9**	**4.5e−9**	−5.3e−10	**−5.1e−9**	−6.1e−10	7.6e-10	−2.4e−10
$\sigma(kb-1)$	1.1e−11	**3.9e−10**	**9.3e−10**	−2.5e−12	**−1.8e−9**	**6.0e−10**	1.2e−10	−5.2e−12

OSD
9, 63–103, 2012

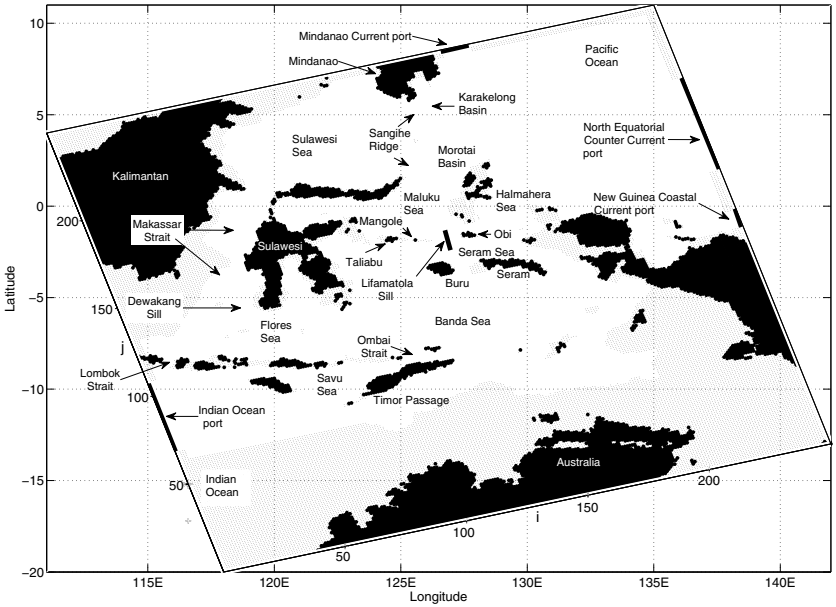

Fig. 1. The model domain location along with names of important topographic features and open ports. The model domain was rotated relative to lines of constant Lat-Lon so that the Indian Ocean port was located on the JADE August 1989 CTD transect between Northwestern Australia and Bali. The model (x, y) domain ranges between i and j values of 1–250, respectively, (see i, j values along model domain edge). Model domain corners in Lat–Lon values are as follows: SW: 20° S 118° E, SE: 13° S 142° E, NE: 11° N 135° E, and NW: 4° N 111° E. The 4 open ports are shown as bold lines along the edge of the model domain. The depth in the grey (dotted) region is less than 100 m. However, the grey region in the Indian Ocean in the southwestern corner of the model domain is greater than 100 m but has been excluded from the model integration to facilitate the Indian Ocean open port. The thick line through the Lifamatola Sill in the North-South direction shows the location of the section discussed in the paper.

OSD
9, 63–103, 2012

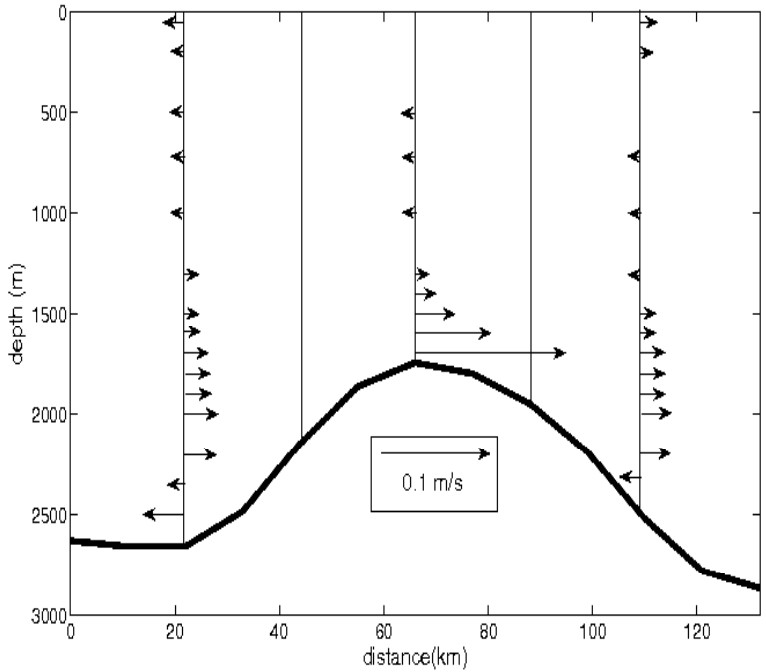

Fig. 2. v-velocities [m s^{-1}] at the section through the Lifamatola passage (at $i = 138$) from north (South Maluku Sea, left, $j = 154$) to south (Seram Sea, right, $j = 146$). See Fig. 1 for i, j coordinates and section location. The five vertical lines show the locations of profiles presented and discussed in the paper. The distance referred to on the abscissa is essentially the distance across the sill from the Maluku Sea in the north to the Seram Sea in the south. The actual sill is located at the shallowest point in the section ($\sim$ 70 km).

OSD
9, 63–103, 2012

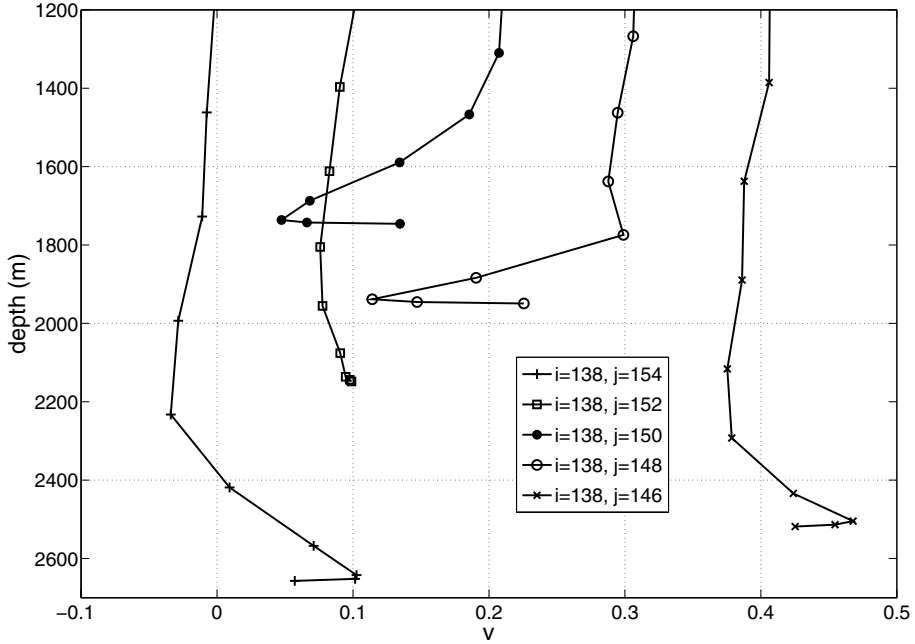

Fig. 3. Profiles of v-component of velocity [m s^{-1}] at the section through the Lifamatola Passage ($i = 138$) from north ($j = 154$, left) to south ($j = 146$, right). Profiles are offset for clarity: for $j = 154$ offset is 0.0 m s^{-1}; for $j = 152$ offset is 0.1 m s^{-1}; for $j = 150$ offset is 0.2 m s^{-1}; for $j = 148$ offset is 0.3 m s^{-1}; for $j = 146$ offset is 0.4 m s^{-1}. See Fig. 1 for i, j coordinates and Fig. 2 for profile locations. Vertical and horizontal lines are shown for convenience.

OSD
9, 63–103, 2012

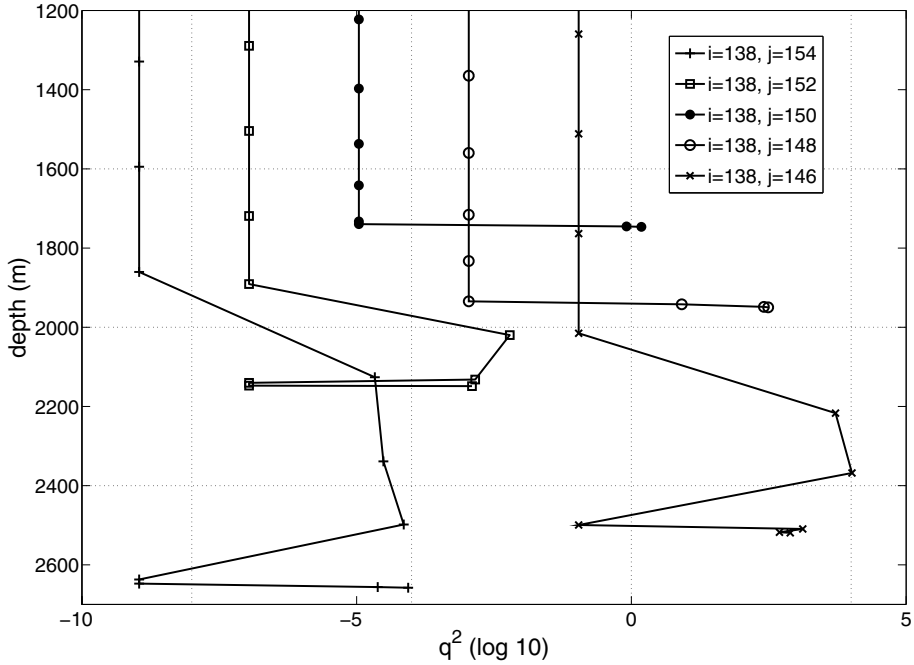

Fig. 4. Profiles of q^2 [m^2 s^{-2}], twice the turbulence kinetic energy (TKE), through the Lifamatola Passage ($i = 138$) from north ($j = 154$) to south ($j = 146$). Decimal logarithmic scale is used along the horizontal axis. Profiles are offset for clarity: for $j = 154$ offset = 0; for $j = 152$ offset = 2 (or q^2 is multiplied by 10^2); for $j = 150$ offset = 4 (or q^2 is multiplied by 10^4); for $j = 148$ offset = 6 (or q^2 is multiplied by 10^6); for $j = 146$ offset = 8 (or q^2 is multiplied by 10^8). See Fig. 1 for i, j coordinates. See Fig. 2 for profile location through sill. Vertical and horizontal lines are shown for convenience.

OSD
9, 63–103, 2012

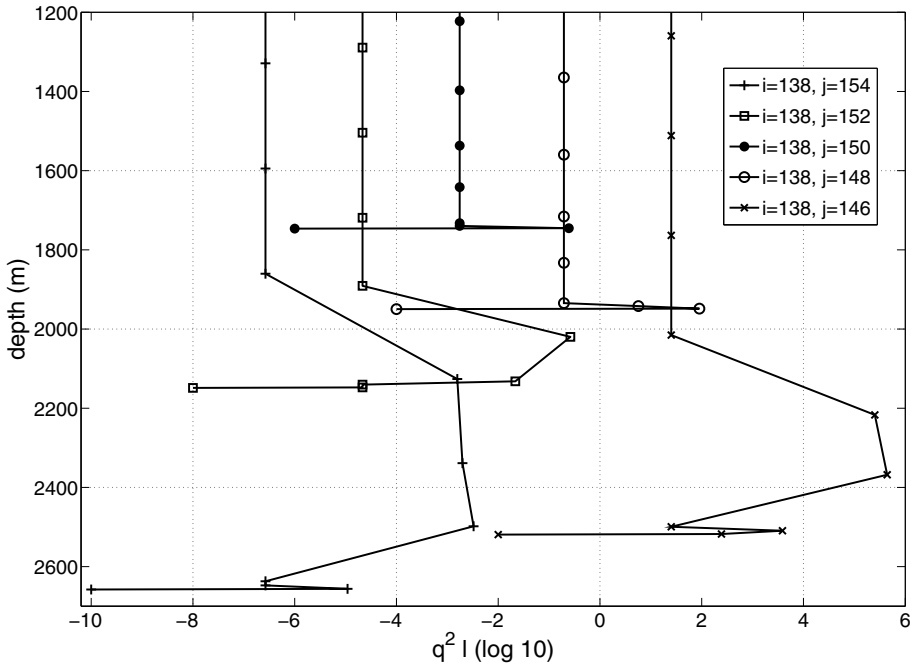

Fig. 5. Profiles of $q^2 l$ [$m^3 s^{-2}$], i.e., twice the TKE times the turbulence length scale. Note that profiles are offset as in Fig. 4.

OSD
9, 63–103, 2012

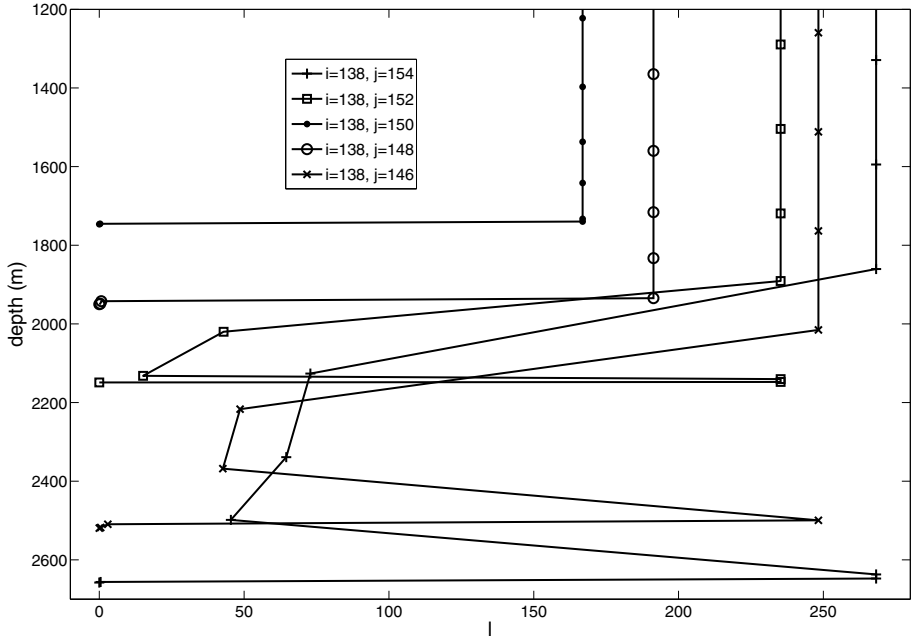

Fig. 6. Turbulence length scale, ℓ [m], for the five profiles considered.

OSD
9, 63–103, 2012

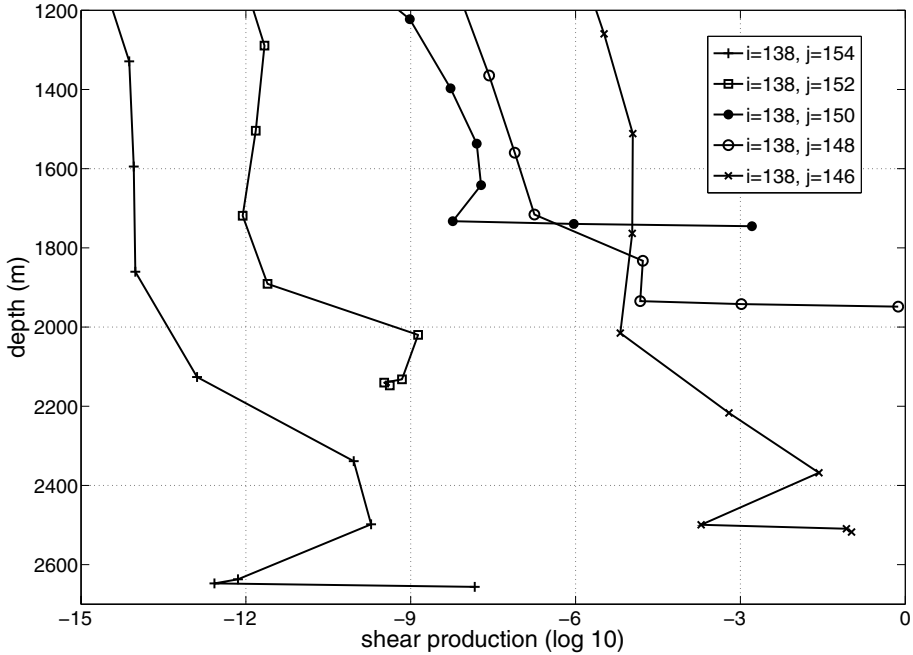

Fig. 7. Profiles of sp, i.e., shear production of TKE [$m^2\,s^{-3}$]. Note that profiles are offset as in Fig. 4.

OSD
9, 63–103, 2012

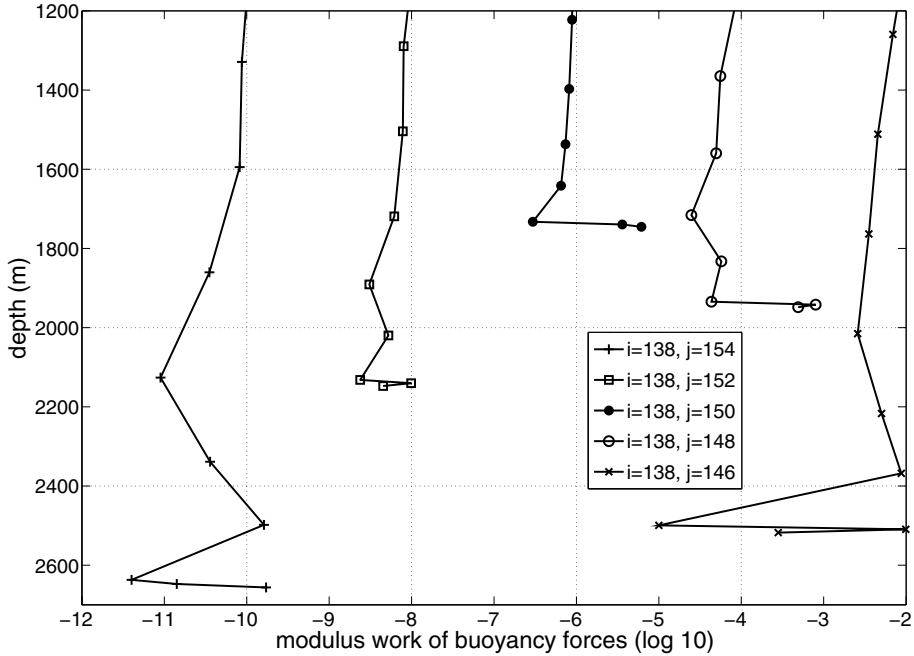

Fig. 8. Profiles of bp, i.e., modulus of work of buoyancy forces or buoyancy production [$m^2\ s^{-3}$]. Note, that values are always negative. Profiles are offset as in Fig. 4.

OSD
9, 63–103, 2012


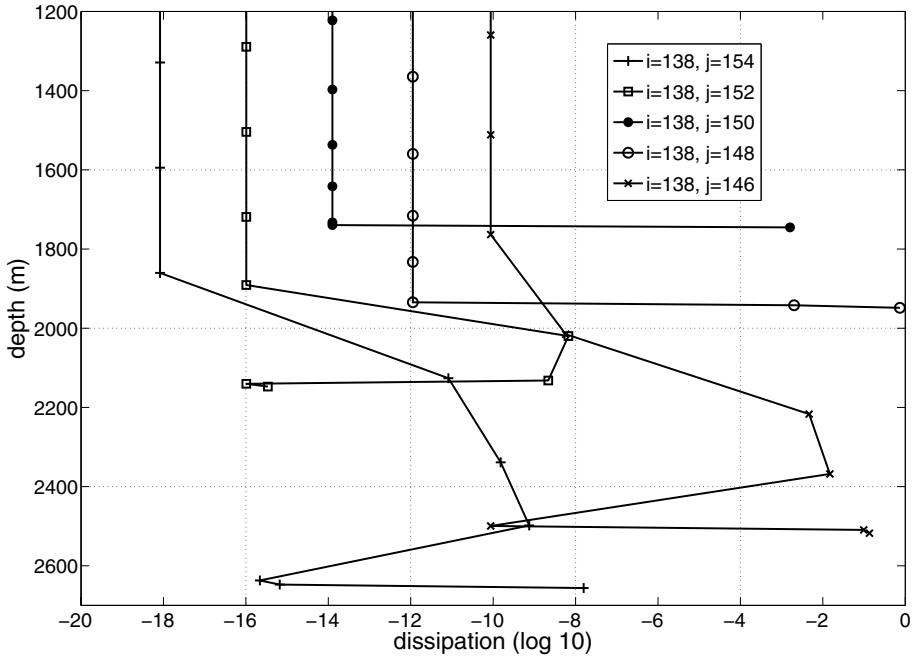

Fig. 9. Profiles of dp, i.e., dissipation of TKE [$m^2\ s^{-3}$]. Profiles are offset as in Fig. 4.

OSD
9, 63–103, 2012

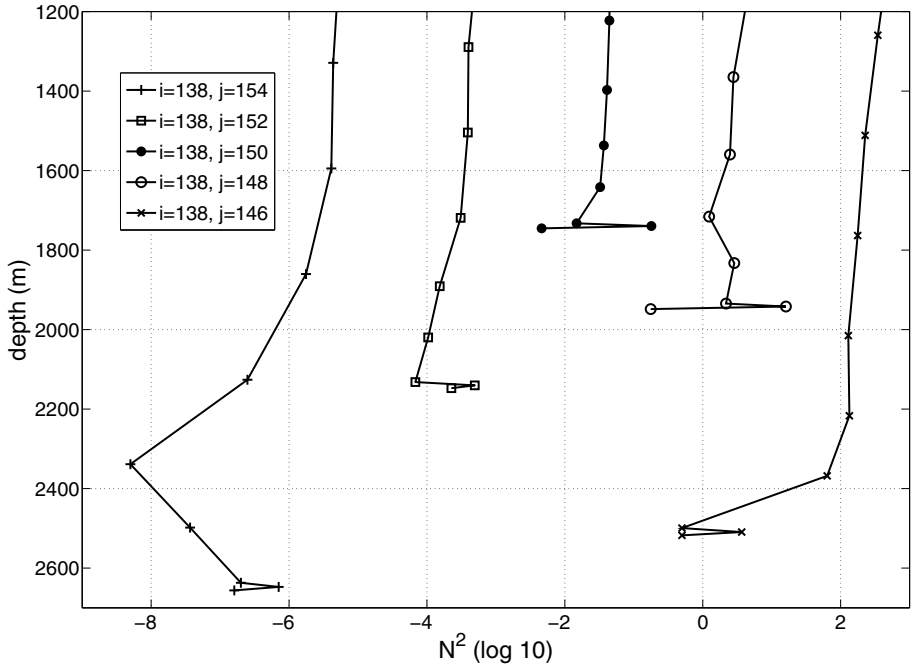

Fig. 10. Profiles of N^2 [s^{-2}], i.e., buoyancy frequency squared. Note that profiles are offset as in Fig. 4.

OSD
9, 63–103, 2012

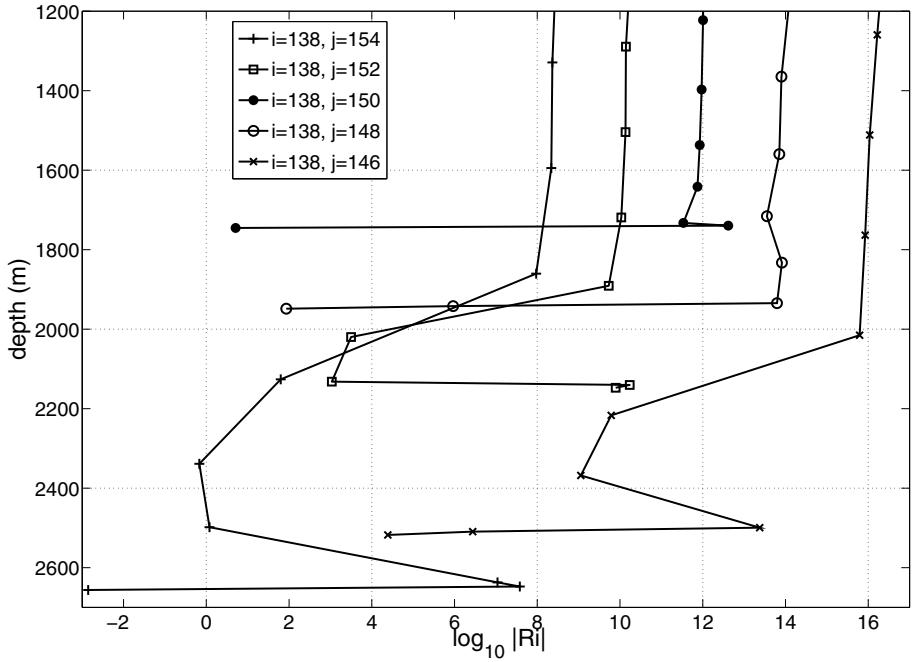

Fig. 11. Profiles of the modulus of the Richardson (Ri) number. Note, all values of the Ri are negative and all profiles are offset as in Fig. 4.

OSD
9, 63–103, 2012

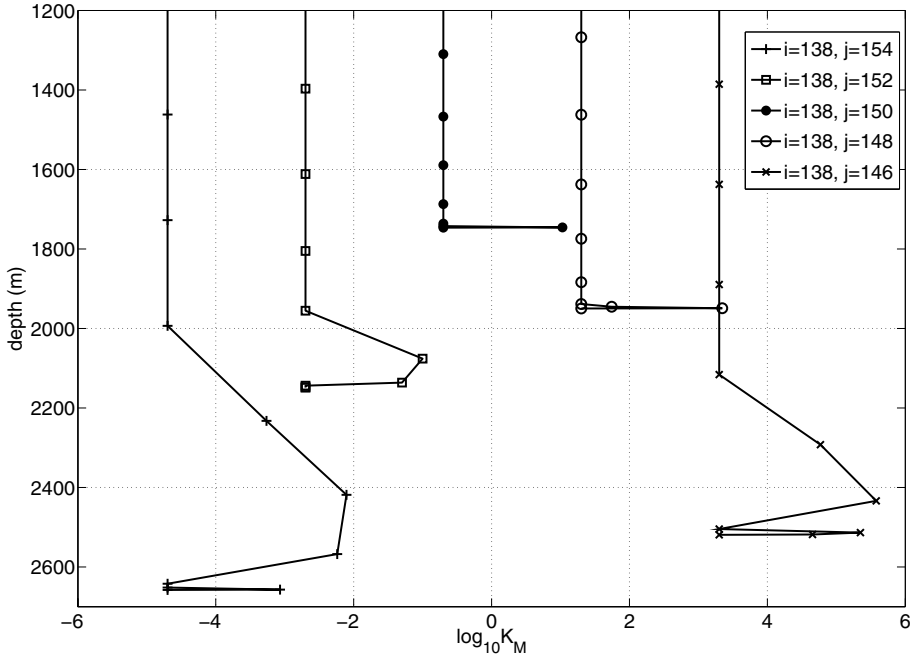

Fig. 12. Profiles of the coefficient of vertical diffusion of momentum, K_M [$m^2\,s^{-1}$]. Profiles are offset as in Fig. 4.

OSD
9, 63–103, 2012

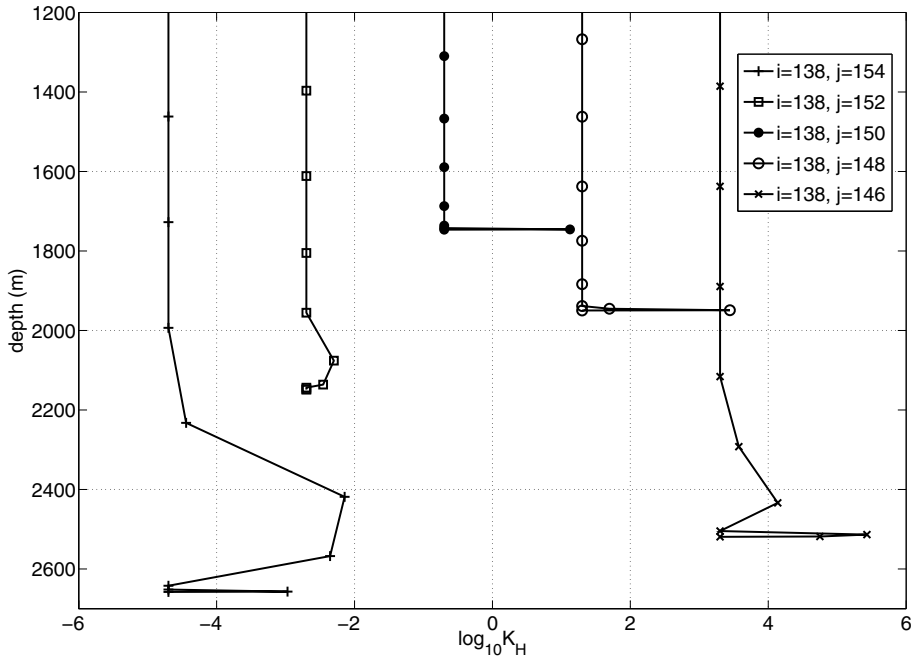

Fig. 13. Profiles of the coefficient of vertical diffusion of temperature or salinity, K_H [$m^2 s^{-1}$]. Profiles are offset as in Fig. 4.

OSD
9, 63–103, 2012

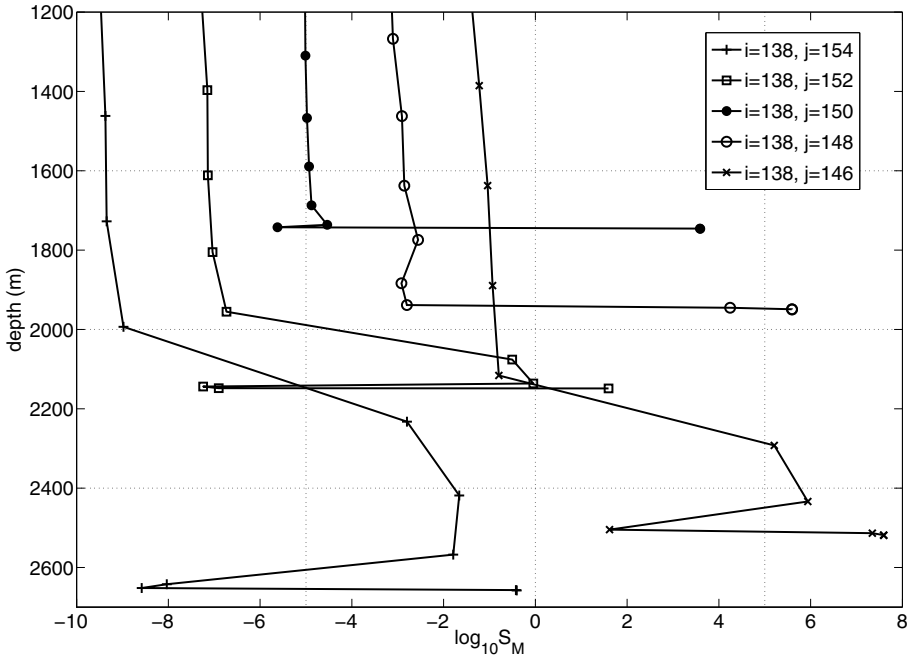

Fig. 14. Profiles of S_M. Profiles are offset as in Fig. 4.

OSD
9, 63–103, 2012

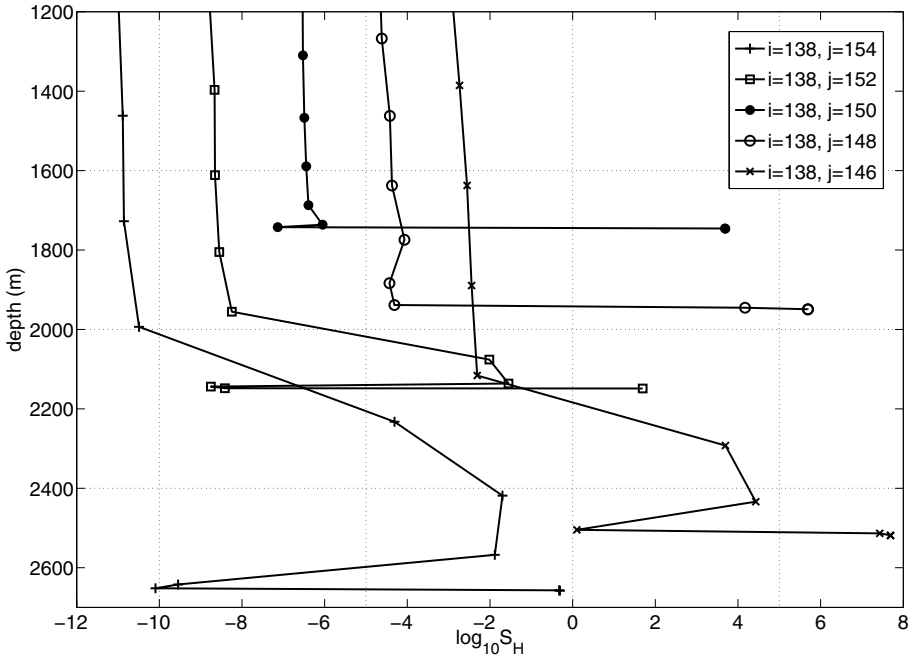

Fig. 15. Profiles of S_H. Profiles are offset as in Fig. 4.

OSD
9, 63–103, 2012